

# One-step Generative Diffusion for Realistic Extreme Image Rescaling

Ce Wang, Zhenyu Hu, Wanjie Sun\*, Zhenzhong Chen  
 School of Remote Sensing and Information Engineering, Wuhan University  
 Wuhan 430079, China

{cewang, zhenyuhu, sunwanjie, zzchen}@whu.edu.cn

## Abstract

Image rescaling aims to learn the optimal low-resolution (LR) image that can be accurately reconstructed to its original high-resolution (HR) counterpart, providing an efficient image processing and storage method for ultra-high definition media. However, extreme downscaling factors pose significant challenges to the upscaling process due to its highly ill-posed nature, causing existing image rescaling methods to struggle in generating semantically correct structures and perceptual friendly textures. In this work, we propose a novel framework called *One-Step Image Rescaling Diffusion (OSIRDiff)* for extreme image rescaling, which performs rescaling operations in the latent space of a pre-trained autoencoder and effectively leverages powerful natural image priors learned by a pre-trained text-to-image diffusion model. Specifically, *OSIRDiff* adopts a pseudo-invertible module to establish the bidirectional mapping between the latent features of the HR image and the target-sized LR image. Then, the rescaled features are refined by a pre-trained diffusion model to generate more faithful and visually pleasing details. The entire model is end-to-end trained to enable the diffusion priors to guide the rescaling process. Considering the spatially non-uniform reconstruction quality of the rescaled latent features, we propose a novel time-step alignment strategy, which can adaptively determine the generative strength of the diffusion model based on the degree of latent reconstruction errors. Extensive experiments demonstrate the superiority of *OSIRDiff* over previous methods in both quantitative and qualitative evaluations. The code will be available at: <https://github.com/xxx/xxx>.

## 1. Introduction

With the explosive growth of ultra high-resolution (HR) images, image rescaling has become essential for enhancing data storage and transmission efficiency [44], optimizing

\*Corresponding author

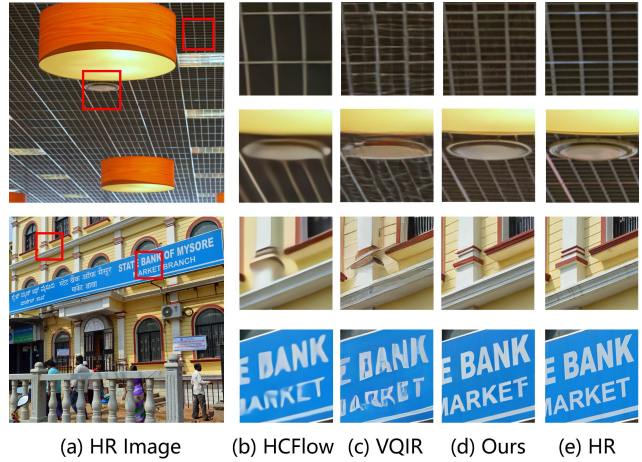


Figure 1. Visual comparison of  $16\times$  image rescaling results.

resource usage in real-time applications [26], and ensuring proper display on devices with varying resolutions [25]. During image rescaling, HR images are downscaled to low-resolution (LR) images for storage, transmission, or display. When HR images are needed, an upscaling process is employed to restore the downscaled images to their original resolution. Unlike image super-resolution (SR) task, image rescaling allows for joint optimization of both downscaling and upscaling processes, preserving detailed information crucial for effective upscaling.

Recently published image rescaling methods can be classified into two main categories: encoder-decoder architecture [14, 31] and invertible neural networks [18, 41]. The encoder-decoder architecture employs two neural networks to perform downscaling and upscaling. While, invertible neural networks view image rescaling as a reversible process, using the forward and backward passes of an invertible neural network to simulate the downscaling and upscaling. Despite the significant improvements in reconstruction quality achieved by these methods, they are limited to small rescaling factors, such as  $2\times$  or  $4\times$ .

However, with the advancement of ultra HR imaging de-

vices, there is an increasing need for extreme rescaling factors (*e.g.*,  $16\times$  or  $32\times$ ) to achieve more efficient storage and transmission of ultra HR data [8, 53]. Existing image rescaling methods often struggle to generate sufficient detail under extreme rescaling factors. Therefore, some approaches propose using pre-trained GANs as priors to constrain the solution space of the reconstructed results. GRAIN [53] and BDFlow [15] use pre-trained StyleGAN [10, 11] to generate high-quality upscaling face images. VQIR [39] leverages the high-quality visual embeddings encapsulated in pre-trained VQGAN [4] to achieve extreme rescaling on natural images. Although these methods have made significant progress in perceptual metrics, we find that their reconstruction results suffer from incorrect semantics and structure. As shown in Fig. 1, although VQIR generates richer details compared to HCFlow, it still fails to reconstruct accurate text and image patterns.

To address the aforementioned issues, we propose a novel framework named One-Step Image Rescaling Diffusion (OSIRDiff) for extreme image rescaling, which performs image rescaling in the latent space of a pre-trained autoencoder and leverages the natural image priors stored in large text-to-image diffusion models to restore HR images. Specifically, first, we use an autoencoder to rescale the latent code of the HR image to the target size, and employ a set of invertible neural networks (INN) to perform the mapping from the feature space to the pixel space to obtain the LR image. Then, the rescaled features are fed into a pre-trained diffusion model to perform a single denoising step, thereby enhancing their perceptual quality. Finally, the entire model is trained end-to-end to allow the diffusion priors to guide the rescaling process. Due to the spatially non-uniform reconstruction quality of the rescaled latent features, different regions of the image require varying levels of generative capability for restoration. Previous studies have shown that the time-step in diffusion models directly controls the generative capacity of the model [35]. Therefore, we propose a time-step alignment mechanism that predicts the appropriate time-step based on the reconstruction quality of the rescaled latent features, thereby achieving a balance between fidelity and realism. As shown in Fig. 1, our model significantly enhances the overall quality of the rescaled images compared to other methods.

Our contributions can be summarized as follows:

- We propose a One-Step Image Rescaling Diffusion framework that performs well in global semantic and structural reconstruction for the extreme image rescaling task.
- We propose a novel decoupled strategy for feature rescaling. It decouples the generation of LR images from the rescaling operation, thereby improving the reconstruction accuracy of the rescaling process.
- We design a time-step alignment strategy to address

the spatially non-uniform reconstruction quality of the rescaled latent features, allowing for more effective utilization of the prior information from the text-to-image diffusion model.

## 2. Related Work

### 2.1. Image Rescaling

Image rescaling aims to downscale HR images to visually coherent LR images and then plausibly reconstruct the original HR images. Unlike image SR, image rescaling involves joint modeling of both downscaling and upscaling processes, leading to higher reconstruction accuracy. Earlier researches [14, 17] utilize CNNs to build an encoder-decoder framework, treating image rescaling as a unified task by jointly training the downscaling and upscaling processes. Instead of directly generating LR images, CAR [31] proposes generating content-adaptive resampling kernels based on HR images to perform the downsampling operation, avoiding pixel-level constraints on the downsampled images. To fully leverage the inherent reversibility of image rescaling, there has been a surge in the use of INNs for this task [16, 43, 48, 54]. IRN [41] is the first invertible framework that models image rescaling as a bijective transformation, embedding residual high-frequency (HF) components into a case-agnostic latent distribution for efficient reconstruction. HCFlow [18] assumes that the HF information depends on the LR image, thereby achieving better performance by incorporating LR conditions in HF information estimation. In extreme image rescaling, generative priors are usually employed to constrain the outcomes. GRAIN [53] and VQIR [39] leverage pre-trained StyleGAN [10, 11] and VQGAN [4], respectively, to achieve notable enhancements in perceptual quality. Nonetheless, these approaches are often limited in image contents, either confined to handling images from specific domains or encountering difficulties when reconstructing faces and textual elements.

Recently, the emergence of the pre-trained Stable Diffusion (SD) model [27] has showcased its efficacy in both content generation [47] and image restoration [34]. Despite this progress, to date, no effort has been made to investigate it within the framework of extreme image rescaling, presenting an unexplored avenue with potential for advancing the field.

### 2.2. Diffusion Model for Image SR

Here, we briefly introduce the application of diffusion models in a related task, *i.e.*, image SR. Diffusion models promote the development of natural image SR in two main ways: training diffusion models from scratch and leveraging pre-trained SD model. The former is represented by SR3 [28], which achieves perceptual quality comparable to GANs. The latter is represented by StableSR [34], which

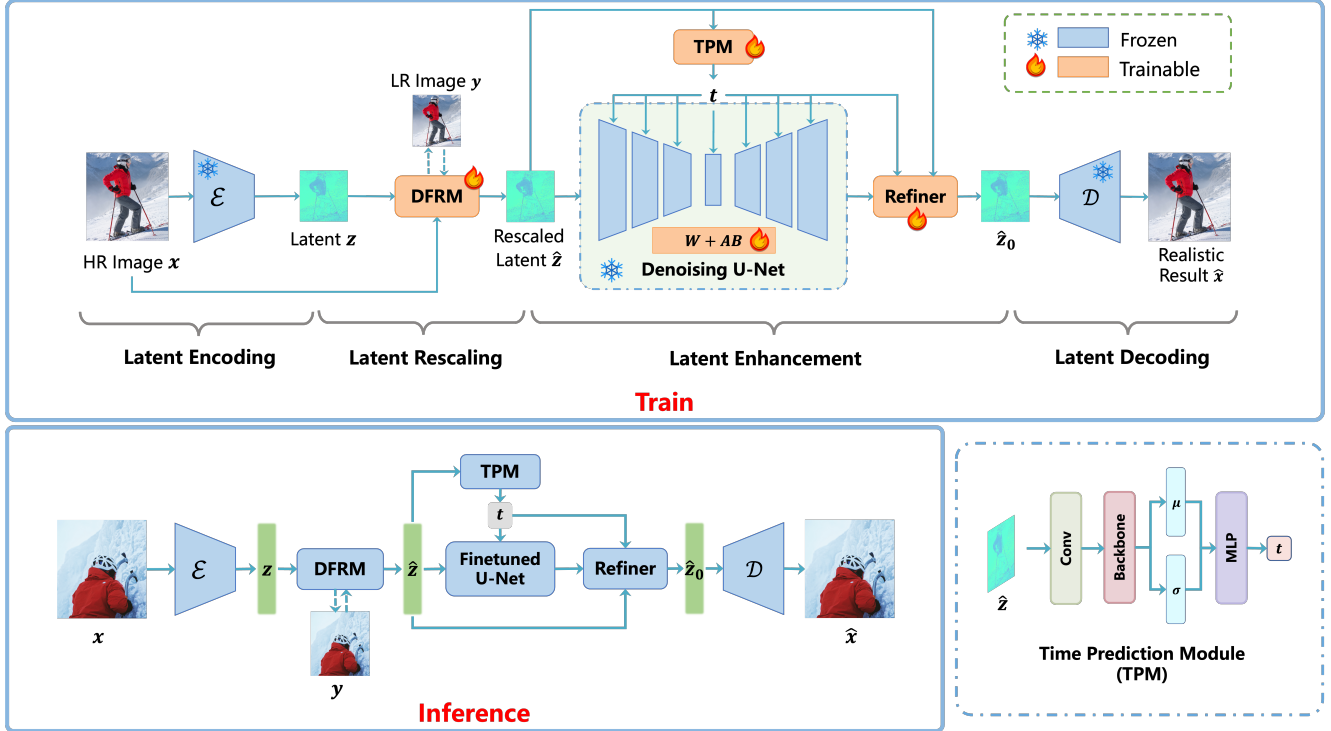


Figure 2. Overview of the proposed One-Step Image Rescaling Diffusion (OSIRDiff). First, the HR images  $x$  are encoded to obtain the latent features  $z$ . These latent features are then rescaled to the target size using the decoupled feature rescaling module (DFRM), producing the LR images  $y$  and outputting the rescaled latent features  $\hat{z}$ . Next, the rescaled latent features  $\hat{z}$  are passed into a pre-trained diffusion model to perform a single denoising step for perceptual enhancement to obtain  $\hat{z}_0$ . Finally, the perceptually enhanced latent features  $\hat{z}_0$  are decoded to obtain the rescaled image  $\hat{x}$ .

aims to build a model capable of handling image restoration under any complex degradation in real-world scenarios. However, due to the inherent difficulty of integrating diffusion models into existing encoder-decoder architectures, few work has yet attempted to combine them with extreme image rescaling. In this work, we decompose extreme image rescaling into two sub-tasks: feature rescaling in the latent space and one-step perception enhancement with the pre-trained SD U-Net.

### 2.3. Diffusion Acceleration

To accelerate the inference process of diffusion models, researchers have proposed various optimization strategies. Fast diffusion samplers [12, 21, 30, 51] effectively reduce the sampling steps required by pre-trained diffusion models, lowering them from the initial thousand steps to as few as 20–50 steps. However, further reductions often lead to substantial performance degradation. Distillation techniques [23, 24, 29, 42, 45, 52] have shown significant promise in accelerating inference. For example, Progressive Distillation [29] minimizes sampling steps to under 10 by training a sequence of student models with progressively increasing stride. InstafLOW [20] advances this further, achieving one-

step generation using reflow and distillation methods. Recently, score-based distillation approaches, including Distribution Matching Distillation [45] and Variational Score Distillation [24], have utilized pre-trained text-to-image diffusion models as distribution matching losses to enable one-step text-to-image generation. Although these methods have made significant strides, high training costs remain a challenge. Inspired by Diffusion2GAN [9], we propose a low-overhead training approach based on Low-Rank Adaptation (LoRA) [6], achieving one-step acceleration for diffusion models and adaptability for image rescaling tasks.

## 3. Methodology

### 3.1. Overview of OSIRDiff

As illustrated in Fig. 2, OSIRDiff consists of four parts: **Latent Encoding**, **Feature Rescaling in the Latent Space**, **One-Step Perception Enhancement** and **Latent Decoding**. First, the input HR images  $x$  are mapped to the latent features  $z$  via the pre-trained VAE encoder  $\mathcal{E}$ . Subsequently, the proposed Decoupled Feature Rescaling Module (DFRM) rescales  $z$  to the target size, outputting LR images  $y$  and the rescaled latent features  $\hat{z}$ . Our aim is to make  $\hat{z}$

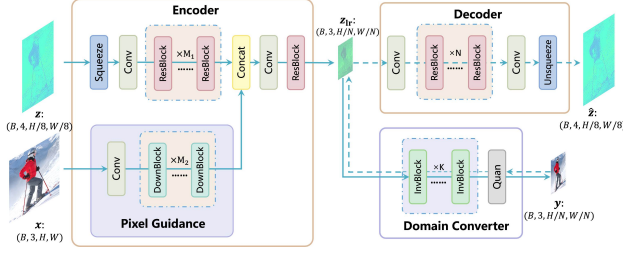


Figure 3. Detailed architecture of Decoupled Feature Rescaling Module (DFRM).

as close as possible to  $z$  so that the rescaled results align with the latent space of the pre-trained VAE, while ensuring that  $y$  and the original HR images  $x$  share the same content. Then, the rescaled features  $\hat{z}$  are fed into a denoising U-Net network to perform a single denoising step to get the perceptually enhanced latent features  $\hat{z}_0$ . Finally, perceptually enhanced latent features  $\hat{z}_0$  are decoded via the pre-trained VAE decoder  $\mathcal{D}$  to obtain the rescaled image  $\hat{x}$ . To dynamically adjust the generative capability based on the reconstruction quality of the rescaled latent features, we design a time-step alignment strategy, which consists of a time-step prediction module (TPM) and a refiner module.

### 3.2. Feature Rescaling in the Latent Space

#### 3.2.1. Network Architecture.

In this part, we perform rescaling of the HR latent features  $z$ , obtaining LR images  $y$  and rescaled features  $\hat{z}$ . A straightforward idea is to construct a transformation chain as  $y = G_e(z)$ ,  $\hat{z} = G_d(y)$ . Here,  $G_e$  is the encoder used to downscale the input features to the target sized LR images, while  $G_d$  represents the decoder used to reconstruct the original HR features. Guidance loss  $\mathcal{L}_{gui.}$  and reconstruction loss  $\mathcal{L}_{rec.}$  are applied to  $y$  and  $\hat{z}$  respectively, to force  $y$  to have the same content as  $x$ , and  $\hat{z}$  to be as similar as possible to  $z$ :

$$\mathcal{L}_{gui.} = \|y - \text{Bicubic}(x)\|_1 \quad (1)$$

$$\mathcal{L}_{rec.} = \|\hat{z} - z\|_1 \quad (2)$$

However, these two losses are contradictory to each other. When the guidance loss approaches zero, the rescaling problem degenerates into a classical SR problem [38], and little information regarding the downscaling process can be embedded into the LR image. In contrast, when the reconstruction loss reaches its global optimum, the rescaling problem degenerates into an image compression problem [22], which results in the LR image lacking any visual content. Therefore, directly applying the guidance loss  $\mathcal{L}_{gui.}$  on  $y$  could adversely impact subsequent upscaling.

Considering the above issues, we devise the DFRM as shown in Fig. 3, which divides the rescaling operation

into two sub-tasks: feature rescaling and LR image generation. Inspired by FGRN [16], we use a set of CNNs to perform downscaling and upscaling, and a separate INN to perform the bidirectional mapping between the feature domain and the pixel domain. To achieve a balance between feature rescaling accuracy and visual quality of LR images, we introduce another pixel guidance module in the encoder to incorporate pixel-level information, which can improve the quality of the LR image. Specifically, DFRM perform feature rescaling through two independent transformation chains  $((x, z) \rightarrow z_{lr} \rightarrow \hat{z}); (z_{lr} \leftrightarrow y)$  as follows:

$$z_{lr} = G_e(x, z) \quad (3)$$

$$z_{lr} \approx F^{-1}(F(z_{lr})) = F^{-1}(y) \quad (4)$$

$$\hat{z} = G_d(z_{lr}) \quad (5)$$

Here,  $F$  and  $F^{-1}$  represent the forward and backward processes of the INN, respectively. Given the latent variable  $z \in R^{\frac{H}{8} \times \frac{W}{8} \times 4}$  of the pre-trained SD VAE as input, the encoder  $G_e$  first transforms it into a compact representation  $z_{lr} \in R^{\frac{H}{N} \times \frac{W}{N} \times 3}$ , whose size is the same as that of the target LR image and  $N$  represents the target downscaling factor. Subsequently, a set of INNs perform the forward process to transform  $z_{lr}$  from the feature domain to the pixel domain and obtain the LR image  $y \in R^{\frac{H}{N} \times \frac{W}{N} \times 3}$  by quantization. Symmetrically, in the upscaling process, the inverse of the INN is used to process the LR image  $y$  and reconstruct  $z_{lr}$ . Finally, the decoder  $G_d$  is utilized to obtain the rescaled feature  $\hat{z}$ .

#### 3.2.2. Loss Function.

Training of this part involves two losses: reconstruction loss and guidance loss. Considering the information lost in quantization operations, the bidirectional mapping between  $z_{lr}$  and  $y$  is not exactly reversible. To ensure the robustness of the network to quantization operations, we consider two types of transformation chains in designing the reconstruction loss:  $(x, z) \rightarrow z_{lr} \rightarrow \hat{z}$  and  $(x, z) \rightarrow z_{lr} \rightarrow y \rightarrow \hat{y}_{lr} \rightarrow \hat{z}$ , which can be expressed as the following formula:

$$\mathcal{L}_{rec.} = \|G_d(G_e(x, z)) - z\|_1 + \|G_d(F^{-1}(F(G_e(x, z)))) - z\|_1 \quad (6)$$

This combination can facilitate the network to reconstruct  $\hat{z}$  with high fidelity in both the existence and absence of quantization operations. Additionally, the guidance loss is designed as follows:

$$\mathcal{L}_{gui.} = \|F(G_e(x, z)) - \text{Bicubic}(x)\|_1 \quad (7)$$

Finally, the loss function of this part is a combination of these two losses:

$$\mathcal{L}_{res.} = \lambda_{rec.}\mathcal{L}_{rec.} + \lambda_{gui.}\mathcal{L}_{gui.} \quad (8)$$

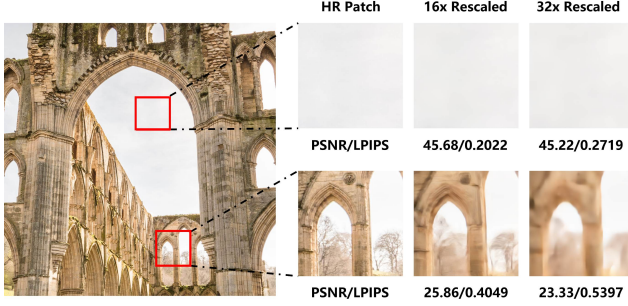


Figure 4. The rescaling operation leads to spatially non-uniform reconstruction quality of the rescaled latent features, which depends on the content of the image and the rescaling factor.

### 3.3. One-Step Perception Enhancement

The latent variable  $\hat{z}$  obtained in Sec. 3.2 retains sufficient semantic information about the HR image, but lacks adequate texture. Therefore, we are proposed to leverage the strong priors stored in the pre-trained SD model to enhance the perceptual quality of the rescaling results in this part. Considering the original diffusion model requires a multi-step iterative sampling algorithm, this significantly increases inference time and makes it difficult to scale to practical applications. Inspired by recent work on accelerating diffusion models [9], we adopt an one-step inference strategy. Specifically, we can directly feed the rescaled latent variable  $\hat{z}$  into the denoising U-Net  $\epsilon = \epsilon_\theta(\hat{z}, t)$  to perform a single denoising step as follows:

$$\hat{z}_0 = \frac{\hat{z} - \sqrt{1 - \bar{\alpha}_t} \epsilon}{\sqrt{\bar{\alpha}_t}} \quad (9)$$

where  $\hat{z}_0$  represents the perceptually enhanced latent features,  $\bar{\alpha}_t$  is the noise scheduler of the forward diffusion process of the SD model, and  $t$  represents the time-step associated with the noise intensity. Finally,  $\hat{z}_0$  can be transformed to the pixel domain through the pre-trained VAE decoder  $\mathcal{D}$  to obtain the upscaled image  $\hat{x}$ :

$$\hat{x} = \mathcal{D}(\hat{z}_0) \quad (10)$$

Then, we can adopt the loss function between  $\hat{x}$  and  $x$  to optimize the U-Net using LoRA layers.

It should be noted that one of the key designs is the selection of the time-step  $t$ . Previous studies [35] have shown that the time-step in diffusion models could determine the trade-off between realism and fidelity. A larger  $t$  results in stronger diversity and greater realism, but at the cost of fidelity. However, we have observed that the quality of the rescaled latent features exhibit non-uniform characteristics, as shown in Fig. 4. After rescaling, the low-frequency regions of an image typically experience less degradation, while the degradation in high-frequency areas

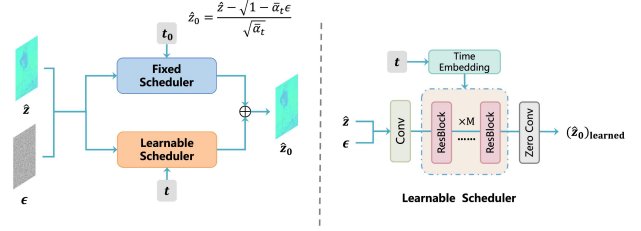


Figure 5. The structure of the refiner module. It combines both the fixed scheduler and learnable scheduler to perform the denoising process. The two schedulers are connected by a zero-convolution layer to stabilize the training.

is more conspicuous, necessitating a higher generative capability for restoration. Thus, we propose to dynamically predict the time-step  $t$  based on the quality of the rescaled latent features. We propose to use a simple yet effective network named time-step prediction module (TPM) to regress  $t$  based on the rescaled latent features:

$$t = \text{TPM}(\hat{z}) \quad (11)$$

Subsequently, the predicted time-step  $t$  is used to perform the single denoising step. During the training phase, we compute a single time-step for each input image patch. In the inference phase, we adopt a tiled inference approach, allowing for predicting different time-steps for various regions of a single image. However, the fixed scheduler used in equation (9) is not differentiable with respect to  $t$ , which prevents gradients from being back-propagated to the TPM. Considering that given  $\hat{z}$ ,  $\epsilon$  and  $t$ , equation (9) essentially represents a linear transformation, which can be learned by a neural network. However, if we simply use a randomly initialized neural network to simulate this process, it would cause the output to deviate significantly from the latent space of the pre-trained VAE, leading to training instability. Therefore, we propose a hybrid refiner module consisting of both a fixed scheduler and a learnable scheduler. The former uses equation (9) to perform the denoising step, while the latter employs a neural network to simulate the denoising scheduler. To ensure training stability, the final layer of the learnable scheduler is a zero-initialized convolution, allowing it to gradually correct the results of the fixed scheduler as training progresses. This process can be described as follows:

$$\hat{z}_0 = \mathcal{S}_{\text{fixed}}(\hat{z}, \epsilon, t_0) + \mathcal{S}_{\text{learned}}(\hat{z}, \epsilon, t) \quad (12)$$

Here  $t_0$  represents the fixed pre-set time-step.

In this part, we fine-tune the denoising U-Net network using LoRA, while also jointly training the TPM and refiner module. To achieve a balance between fidelity and realism, we supervise the reconstruction results  $\hat{x}$  using pixel loss

Table 1. Quantitative comparisons with different methods at 16× and 32×. The symbols ↑ and ↓ respectively represent that higher or lower values indicate better performance. Bold represents the best and underline represents the second best.

Dataset	Method	PSNR ↑		SSIM ↑		LPIPS ↓		DISTS ↓		MUSIQ ↑		CLIQQA ↑	
		16×	32×	16×	32×	16×	32×	16×	32×	16×	32×	16×	32×
DIV2K	EDSR	24.64	22.13	0.6572	0.6056	0.5376	0.6219	0.3162	0.4184	34.15	23.28	0.3397	0.4193
	RCAN	24.34	22.06	0.6479	0.6034	0.5485	0.6307	0.3269	0.4349	31.57	23.18	0.3408	0.4091
	ESRGAN	23.15	21.15	0.5946	0.5808	0.4478	0.5788	0.2378	0.4237	59.80	43.40	0.6161	0.3725
	IRN	<u>26.04</u>	<u>22.84</u>	<u>0.7020</u>	<u>0.6212</u>	0.5153	0.6095	0.3041	0.4036	43.72	28.70	0.2799	0.2336
	HCFlow	<b>26.66</b>	<b>23.89</b>	<b>0.7176</b>	<b>0.6467</b>	0.4885	0.5816	0.2866	0.3852	46.43	37.25	0.2735	0.2792
	VQIR	23.91	22.02	0.6498	0.5823	<u>0.3174</u>	<u>0.4568</u>	<u>0.1024</u>	<u>0.2663</u>	<u>64.04</u>	<u>58.21</u>	<u>0.6350</u>	<u>0.6293</u>
	Ours	23.77	22.10	0.6675	0.5839	<b>0.3026</b>	<b>0.4281</b>	<b>0.0824</b>	<b>0.1597</b>	<b>66.31</b>	<b>65.51</b>	<b>0.6443</b>	<b>0.6521</b>
Urban100	EDSR	19.93	18.08	0.5020	0.4447	0.5827	0.6839	0.3701	0.4734	41.97	24.80	0.3439	0.4173
	RCAN	19.96	18.14	0.5017	0.4452	0.5859	0.6880	0.3745	0.4808	40.31	24.46	0.3561	0.4130
	ESRGAN	19.36	17.68	0.4835	0.4344	0.4741	0.6142	0.2554	0.4288	65.82	57.02	0.5849	0.3860
	IRN	<u>22.15</u>	<u>18.93</u>	0.6155	<u>0.4772</u>	0.5114	0.6567	0.3338	0.4457	58.73	32.03	0.3217	0.2210
	HCFlow	<b>22.59</b>	<b>19.86</b>	<u>0.6335</u>	<b>0.5185</b>	0.4841	0.6048	0.3125	0.4101	60.62	47.94	0.3182	0.2827
	VQIR	20.27	18.44	0.5782	0.4427	<u>0.3038</u>	<u>0.5045</u>	<u>0.1418</u>	<u>0.3290</u>	<u>71.56</u>	<u>61.64</u>	<u>0.6619</u>	<u>0.6568</u>
	Ours	21.34	18.77	<b>0.6464</b>	0.4655	<b>0.2601</b>	<b>0.4490</b>	<b>0.1107</b>	<b>0.2265</b>	<b>72.21</b>	<b>71.03</b>	<b>0.6773</b>	<b>0.6643</b>
CLIC2020	EDSR	26.33	23.92	0.7408	0.7062	0.5109	0.5742	0.3057	0.4024	33.17	21.77	0.3392	0.4307
	RCAN	26.37	24.04	0.7407	0.7072	0.5133	0.5777	0.3126	0.4151	31.59	22.07	0.3469	0.4180
	ESRGAN	25.43	23.48	0.7018	0.6991	0.4213	0.5347	0.2209	0.4014	57.80	40.98	<u>0.6107</u>	0.3537
	IRN	<u>28.55</u>	<u>24.93</u>	<u>0.7907</u>	<u>0.7228</u>	0.4676	0.5528	0.2746	0.3776	47.66	27.81	0.2950	0.2495
	HCFlow	<b>28.82</b>	<b>26.21</b>	<b>0.7949</b>	<b>0.7451</b>	0.4542	0.5325	0.2635	0.3611	47.72	37.15	0.2733	0.2884
	VQIR	25.69	24.12	0.7363	0.6942	<u>0.2854</u>	<u>0.4191</u>	<u>0.0901</u>	<u>0.2445</u>	<u>64.36</u>	<u>54.83</u>	0.6105	<u>0.6068</u>
	Ours	25.81	24.16	0.7497	0.6887	<b>0.2777</b>	<b>0.3968</b>	<b>0.0754</b>	<b>0.1459</b>	<b>65.84</b>	<b>64.38</b>	<b>0.6198</b>	<b>0.6586</b>
DIV8K	EDSR	26.56	24.48	0.6776	0.6472	0.5437	0.6048	0.3358	0.4325	30.83	22.30	0.3701	0.4686
	RCAN	26.63	24.57	0.6778	0.6481	0.5470	0.6085	0.3430	0.4449	29.93	22.52	0.3796	0.4502
	ESRGAN	25.49	23.78	0.6247	0.6350	0.4628	0.5610	0.2518	0.4268	53.49	39.11	<u>0.6401</u>	0.4078
	IRN	<u>28.95</u>	<u>25.46</u>	<u>0.7402</u>	<u>0.6636</u>	0.4932	0.5870	0.3044	0.4066	42.61	27.76	0.3216	0.2741
	HCFlow	<b>29.22</b>	<b>26.69</b>	<b>0.7470</b>	<b>0.6857</b>	0.4793	0.5616	0.2932	0.3906	42.71	35.53	0.2948	0.3128
	VQIR	25.79	24.26	0.6889	0.6350	<u>0.3221</u>	<u>0.4457</u>	<u>0.1066</u>	<u>0.2628</u>	56.76	51.44	0.5769	<u>0.6203</u>
	Ours	25.93	24.15	0.7107	0.6302	<b>0.3198</b>	<b>0.4376</b>	<b>0.0927</b>	<b>0.1798</b>	<b>57.75</b>	<b>58.89</b>	<b>0.6598</b>	<b>0.6461</b>

and perceptual loss as follows:

$$\mathcal{L}_{\text{enh.}} = \underbrace{\|\hat{x} - x\|_1}_{\text{pixel loss}} + \underbrace{\lambda_{\text{lips}} \mathcal{L}_{\text{lips}}(\hat{x}, x) + \lambda_{\text{dists}} \mathcal{L}_{\text{dists}}(\hat{x}, x)}_{\text{perceptual loss}} \quad (13)$$

## 4. Experiments

### 4.1. Experimental Setup

#### 4.1.1. Datasets and Evaluation Metrics.

We train the proposed OSIRDiff using the DF2K dataset [1, 19]. Considering that traditional benchmarks such as Set5, Set14, and BSD100 often have lower quality and resolution [5], they are not suitable for evaluating extreme rescaling methods. Therefore, we utilize four high-resolution datasets: DIV2K, Urban100 [7], CLIC2020 [32], and DIV8K [5] to evaluate models been compared. We adopt PSNR and SSIM [37] for quantitative evaluation. For perceptual quality evaluation, reference-based metrics LPIPS [49] and DISTS [3] are used. For non-reference im-

age quality assessment, we use metrics including MUSIQ [13] and CLIQQA [33].

#### 4.1.2. Training Details

OSIRDiff is built based on the SD 2.1-base model, and the training is divided into three stages. First, we train the DFRM using equation (8). Then we adopt equation (13) to jointly train the LoRA layers, the TPM and the refiner module. Finally, we use a smaller learning rate to jointly fine-tune DFRM, LoRA layers, TPM and refiner module using a combination of equations (8) and (13). More training details are provided in the supplementary material.

## 4.2. Results and Comparison with SOTA

We compare the proposed OSIRDiff with three kinds of methods: (1) bicubic downscaling and SR, *i.e.*, EDSR [19], RCAN [50] and ESRGAN [36]; (2) flow-based rescaling models, *i.e.*, IRN [41] and HCFlow [18]; (3) prior-based extreme rescaling method VQIR [39]. Some of them are proposed for 4× rescaling factors and we extended them to 16× or 32×. To ensure a fair comparison, all methods are

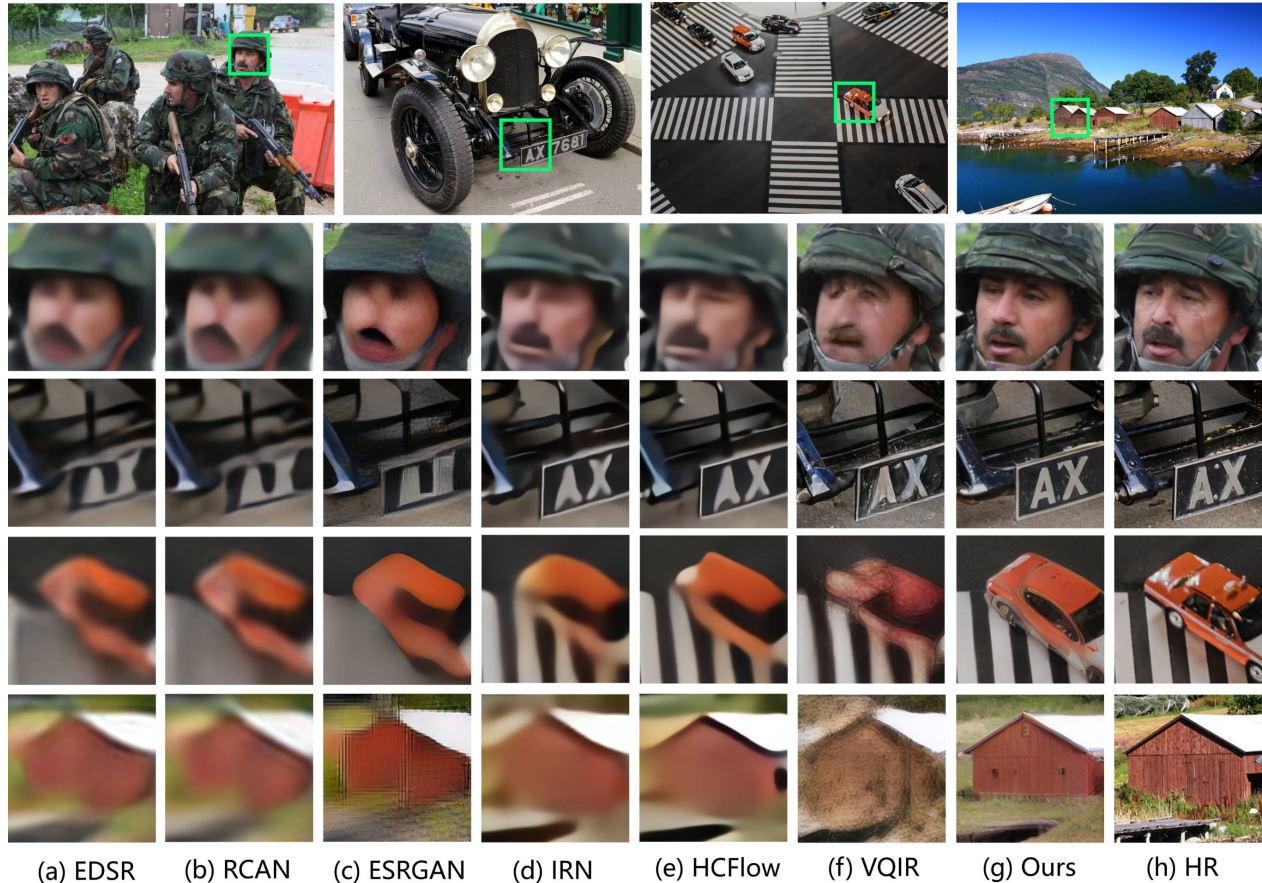


Figure 6. Qualitative comparisons of  $16\times$  (the 2nd and 3rd rows) and  $32\times$  (the 4th and 5th rows) rescaling results. The first row represents the original high-resolution images. Our method achieves higher semantic accuracy, such as more recognizable faces, clearer text, and more realistic structures.

trained until convergence on the DF2K dataset following their original configurations.

#### 4.2.1. Quantitative Results

Table 1 presents the  $16\times$  and  $32\times$  quantitative image rescaling results on four datasets. The performance of SR methods are generally poor. While methods based on INNs (HCFlow and IRN) achieve the highest PSNR and SSIM due to its consideration of the correlation between downscaling and upscaling. In generative methods, VQIR achieves relatively good perceptual metrics by leveraging the priors of the pre-trained VQGAN. In contrast, our method achieves optimal performance across all perceptual metrics on all datasets. For instance, in the  $32\times$  rescaling on the DIV2K validation set, our method improves the DISTS metric by 40.03% compared to the second-best VQIR. Moreover, in the  $16\times$  rescaling on the Urban100 dataset, SSIM of our method even surpasses that of the INN-based regression model, reaching optimal performance. This demonstrates the advantage of our method

in reconstructing the structure of images.

#### 4.2.2. Qualitative Results

In Fig. 6, we present visual comparisons at  $16\times$  and  $32\times$  rescaling factors. Due to the ill-posed nature of extreme rescaling, pixel-oriented optimization methods such as EDSR, RCAN, IRN, and HCFlow produce overly-smoothed results. Although ESRGAN incorporates perceptual optimization it still cannot generate adequate details. VQIR leverages the pre-trained VQGAN as a prior, allowing it to generate rich details and sharp edges. However, it struggles with faces and more complex structures. Thanks to the powerful prior provided by the pre-trained SD and the rich semantic information contained in the latent space of the pre-trained VAE, our method effectively addresses these issues. It not only generates sufficiently rich textures but also reconstructs accuracy semantics and regular structures, such as faces, text and architectural structures.

The quantitative experiments demonstrate that our model exhibits superior performance on the Urban100 [7] dataset,

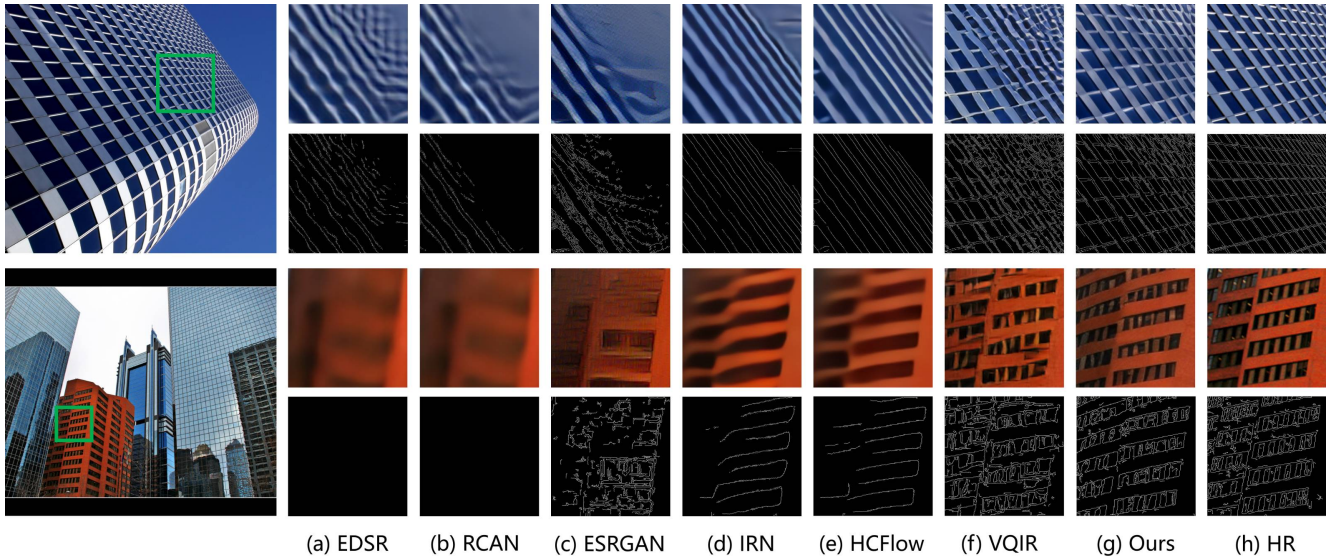


Figure 7. Visual comparisons of  $16\times$  rescaling methods on the Urban100 dataset, including both the rescaled images and corresponding edge maps. Our model is capable of restoring more regular structures and producing sharper, more accurate edges.

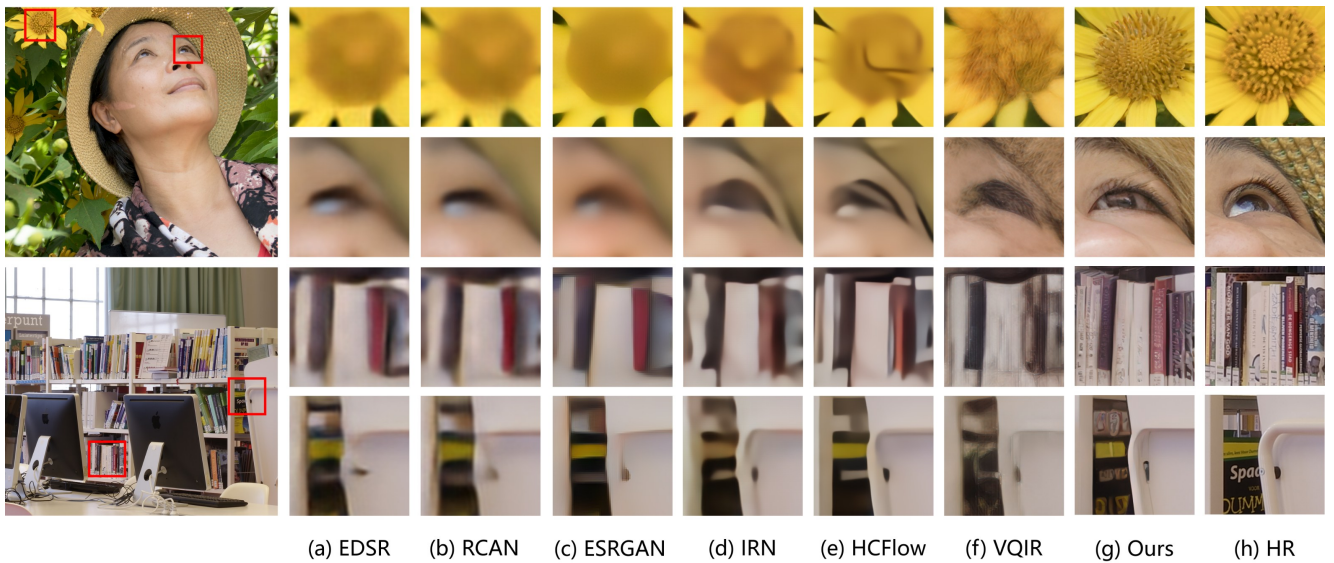


Figure 8. Visual comparisons of  $32\times$  rescaling methods on the DIV8K dataset

confirming that our method produces more accurate structural features. In this section, we provide a visual comparison of  $16\times$  rescaling results on the Urban100 dataset, as shown in Fig. 7. Traditional regression models, such as EDSR [19], RCAN [50], IRN [41], and HCFlow [18], tend to generate overly-smooth results. GAN-based methods, including ESRGAN [36] and VQIR [39], generate more details, but their edge information lacks accuracy and regularity. In contrast, our approach, by leveraging the prior knowledge encapsulated in the SD model, is able to reconstruct more accurate and rich edge details. In Fig. 8, we

present a visual comparison of  $32\times$  rescaling results on the ultra-high-resolution dataset, DIV8K [5]. It is evident that our method is capable of recovering images with accurate semantics, even at extreme upscaling factors.

To validate the effectiveness of our downscaling scheme, we conduct a visual comparison of the downsampled LR images with state-of-the-art (SOTA) methods, as shown in Fig. 9. Overall, the LR images generated by our method achieve comparable or even superior visual quality to SOTA image rescaling methods. The LR images produced by VQIR exhibit noticeable color shifts. Furthermore, VQIR generated



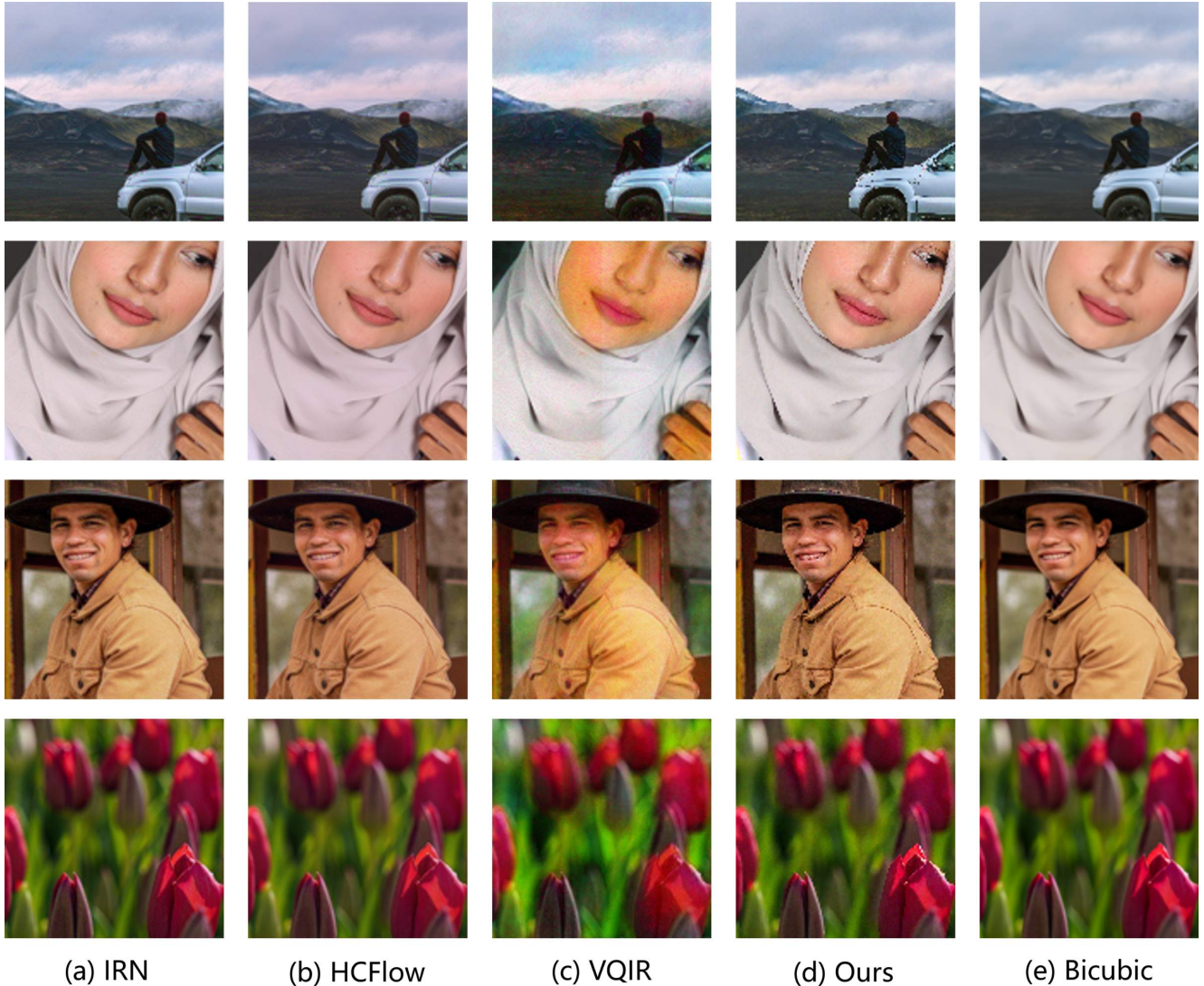


Figure 9. Visual comparisons of downscaled LR images with sota methods.

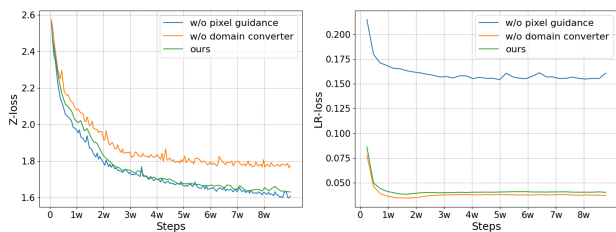


Figure 10. The validation loss curves when removing a specific component from the DFRM.

LR images contain significant noise, whereas our method exhibits a certain degree of ringing artifacts. In future work, we plan to further optimize the quality of the LR images.

### 4.3. Ablation Study

We conduct ablation experiments to validate the effectiveness of each component. All ablations are trained on the DF2K dataset and tested on the validation set of the DIV2K.

#### 4.3.1. Effectiveness of Feature Rescaling

To verify the effectiveness of the feature rescaling operation, we move the rescaling operation from the latent space to the pixel space. Specifically, we use HCFlow [18], the comparative method with the best PSNR performance, to perform the rescaling operation in the pixel domain, followed by perceptual enhancement using the same approach described in Sec. 3.3. As shown in Fig. 11, the rescaling operator in pixel space takes HR image as input and simultaneously outputs both the LR image and the rescaled

image. Then, to use SD for perceptual enhancement, we need to map the rescaled image to the latent space using a VAE encoder and perform the denoising process. Finally, the enhanced latent features are mapped back to the pixel space using the VAE decoder. Due to the nonlinear mapping nature of the VAE encoder, the minimum distance in pixel space does not correspond to the minimum distance in latent space. This causes the rescaling operator trained in pixel space to misalign with the prior of the pre-trained SD model, resulting in a degradation of perceptual quality. As shown the 1st row in Table 2, the rescaling operation in the latent space can improve reconstruction performance, as evidenced by much lower LPIPS and DISTs.

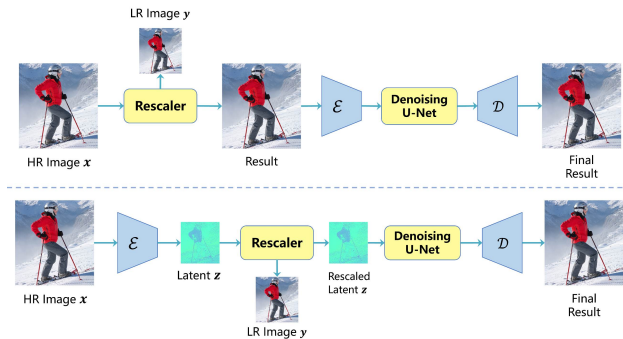


Figure 11. Image rescaling within pixel space and latent space with Stable Diffusion (SD) prior.

As shown in Fig. 12, we conduct visual comparisons between rescaling in latent space and pixel space in two different scenarios. Our latent-space rescaling method is able to reconstruct more realistic textures and more accurate structural features. This indicates that latent-space rescaling operation can preserve sufficiently fine-grained contextual information about the HR image, such as structure, texture, and semantics.

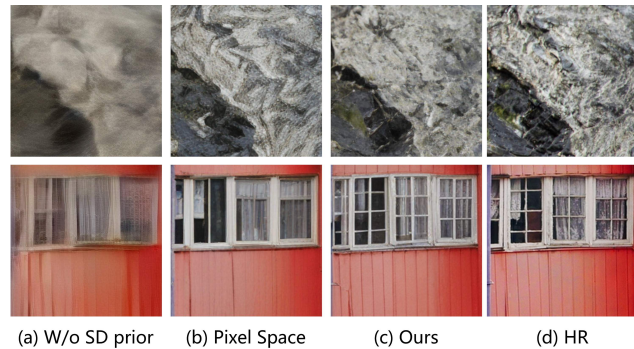


Figure 12. Visual comparisons of our method with rescaling in pixel space and without the SD prior.

Table 2. Ablation study of rescaling space and SD prior.

Latent space	Pixel space	SD prior	LPIPS ↓	DISTS ↓
×	✓	✓	0.3630	0.1154
✓	×	×	0.4675	0.3109
✓	×	✓	<b>0.3026</b>	<b>0.0824</b>

### 4.3.2. Necessity of SD Prior

To validate that SD model provides rich priors about real-world HR images, we directly omit the perceptual enhancement part. As shown in Table 2 (2nd row), the introduction of the SD priors can significantly improve performance of LPIPS and DISTs and greatly enhance the perceptual quality of the reconstruction results. Here, we compare the latent features before and after perceptual enhancement by decoding them to the pixel space using the VAE decoder, as shown in Fig. 12. It can be seen that the latent features before perceptual optimization exhibit noticeable color shifts and blurriness when mapped to the pixel domain. In contrast, the perceptually enhanced latent features display richer textures and more accurate color information. Therefore, leveraging the rich natural image priors in the pre-trained Stable Diffusion model can significantly enhance the visual quality of rescaled images.

### 4.3.3. Effectiveness of DFRM Design

Our DFRM includes two specific designs: the domain converter module and the pixel guidance module. To analyze their impact, we remove each component individually and plot the validation loss curves, as shown in Fig. 10. It can be observed that the introduction of the INN can reduce reconstruction error. Although the pixel guidance module does not improve reconstruction performance, our experiments show that it can enhance the fidelity and visual quality of the LR images, as demonstrated by the lower guidance loss in Fig. 10. As shown in Fig. 13, the LR images exhibit significant noise and color distortions in the absence of pixel guidance. However, the introduction of pixel guidance significantly alleviates these issues. Therefore, the design of our DFRM strikes a good balance between feature reconstruction and LR image quality.

### 4.3.4. Effectiveness of Time Alignment

To validate the effectiveness of our proposed time-step alignment strategy, we retrain our model using fixed time-steps. This involves removing the TPM and refiner modules and employing a manually selected time-step to perform a single denoising step based on equation (9). Following the setting of previous work [40], we select fixed time-steps 1 and 999 for comparison. As shown in Fig. 14, when the time-step is set to a smaller value, the model achieves higher fidelity but lower perceptual quality, and the situation is reversed when a larger time-step is chosen. In contrast, our

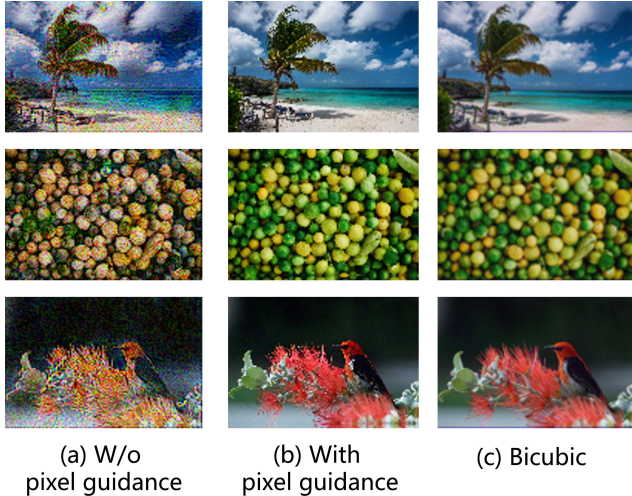


Figure 13. Visual comparisons of LR images with and without pixel guidance.

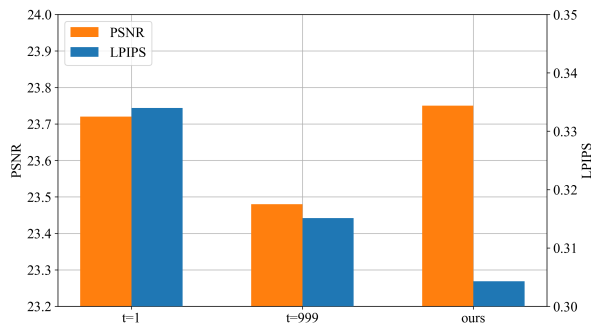


Figure 14. Ablation study about time alignment.

time-step alignment mechanism can dynamically determine the level of generative capability based on the image content, thereby achieving optimal performance in both fidelity and perceptual quality.

## 5. Discussions

### 5.1. Comparison with JPEG Compression

Our model can be combined with existing lossless image compression methods to achieve extreme compression ratios. To validate this, we use the lossless compression image format PNG to compress LR images and compare its performance with JPEG compression at various bit-rates. As shown in Fig. 15, at the same bits per pixel (bpp), the image reconstruction quality of our model significantly surpasses that of the JPEG compression. These comparisons demonstrate the potential of our model for image compression.

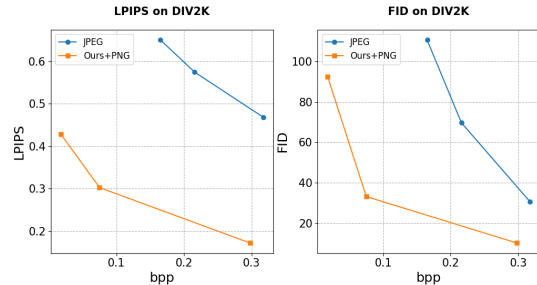


Figure 15. R-D curves of JPEG compression and our proposed model on the DIV2K validation set.

In Fig. 16, we present the visual quality, the bpp and the LPIPS of the reconstructed images. Compared to JPEG compression, our method requires comparable or less storage space while achieving superior objective metrics. Additionally, JPEG compression tends to produce noticeable block artifacts and color distortions in the background regions of the images, whereas our model maintains superior reconstruction quality across all three scales.

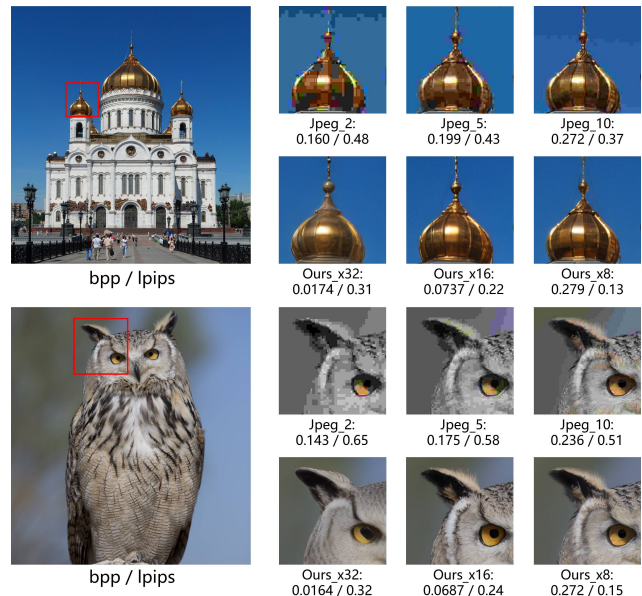


Figure 16. Visual comparisons between our model and JPEG compression. bpp/LPIPS of the reconstructed images are shown below the images.

### 5.2. Time-step Distribution

To overcome the non-uniform degradation introduced by the rescaling operation, we design a time-step alignment strategy to predict an optimal time-step  $t$  based on the degraded latent variable  $\hat{z}$ , enabling dynamic allocation of generative capability. During the inference phase, our model can perform tiled inference, allowing it to predict dif-

ferent time-steps for various regions of the same image. We discuss the distribution of time-steps at both the single image and dataset scales.

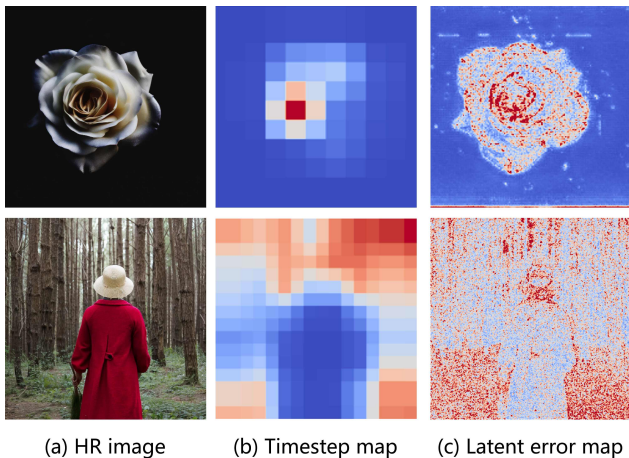


Figure 17. The time-steps  $t$  predicted by the TPM on a single image, along with the corresponding latent variable rescaling error map  $|z - \hat{z}|$ .

First, we visualize the time-steps corresponding to different regions of the image shown in Fig. 17. We also present the latent variable rescaling error map  $|z - \hat{z}|$  for comparison. It can be observed that in more complex regions, the rescaling operation introduces larger errors. Correspondingly, these areas also require larger time-steps. This is because complex regions necessitate greater generative capability for restoration.

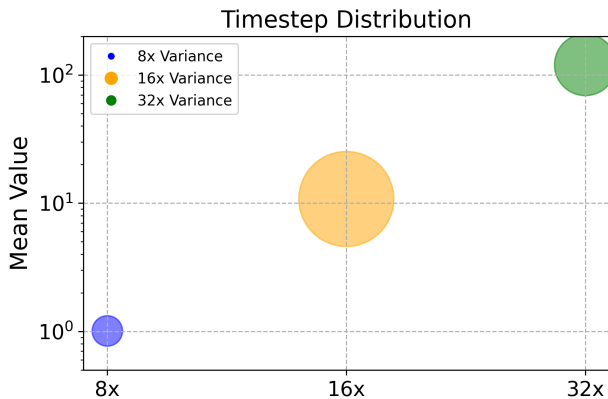


Figure 18. The distribution of time-steps predicted by the TPM on the DIV2K validation set at different rescaling scale factors. Smaller scale factor results in smaller time-steps.

Next, we present the distribution of predicted time-steps at different rescaling scales on the DIV2K validation set shown in Fig. 18. The vertical axis and the size of the bubbles represent the mean and variance of the time-steps, re-

Table 3. The performance comparison between our  $4\times$  rescaling model and VAE.

Method	PSNR $\uparrow$	LPIPS $\downarrow$	MUSIQ $\uparrow$	CLIPQA $\uparrow$
VAE	29.00	0.1570	<b>65.54</b>	0.6234
Ours- $4\times$	<b>29.32</b>	<b>0.1456</b>	65.47	<b>0.6313</b>

spectively. It can be observed that the mean of the predicted time-steps increases as the rescaling scale becomes larger. This is because larger rescaling scales result in greater image degradation, necessitating stronger generative capability for restoration. Additionally, we find that the predicted time-steps for the  $16\times$  rescaling exhibit the largest variance. This indicates that  $16\times$  rescaling is a task that balances both fidelity and generative capacity. In contrast,  $8\times$  rescaling tends to prioritize fidelity, while  $32\times$  rescaling leans more towards generative capabilities.

## 6. Limitations

### 6.1. Upper Bound of OSIRDiff

Since our method performs the rescaling operation in the latent space of a pre-trained VAE, its performance ceiling is inherently constrained by the VAE itself. The VAE encoding is a lossy process and can be described as follows:

$$z = \mathcal{E}(x) \quad (14)$$

Here,  $x \in R^{H \times W \times 3}$  represents original HR image and  $z \in R^{\frac{H}{8} \times \frac{W}{8} \times 4}$  represents corresponding latent features. We can measure the compression rate from the perspective of the number of bits:

$$\begin{aligned} \text{Bits}(x) &= \text{Size}(x) \times \text{Bits}(\text{uint8}) \\ &= (H \times W \times 3) \times 8 \end{aligned} \quad (15)$$

$$\begin{aligned} \text{Bits}(z) &= \text{Size}(z) \times \text{Bits}(\text{float16}) \\ &= \left( \frac{H}{8} \times \frac{W}{8} \times 4 \right) \times 16 \end{aligned} \quad (16)$$

$$\text{Rate} = \frac{\text{Bits}(z)}{\text{Bits}(x)} = \frac{1}{24} \quad (17)$$

It can be observed that VAE encoding can be regarded as a compression process with a compression ratio of 24. From the perspective of rescaling, this is equivalent to a rescaling operation with a scale factor of  $S = \sqrt{24}$ . Any rescaling scale smaller than  $S$  will inevitably be limited by the reconstruction performance of VAE, as the VAE encoding process has already discarded significant amounts of information.

Furthermore, we directly encode and decode input HR images using VAE without performing any rescaling operations, representing the upper performance bound of our model. Additionally, we train an OSIRDiff model for  $4\times$

rescaling and compare its performance with the reconstruction capability of the VAE, as illustrated in Table 3. It can be observed that the performance of our  $4\times$  rescaling model is very close to the reconstruction performance of the VAE, indicating that the rescaling performance at this scale is limited by the VAE reconstruction capacity. This also highlights a potential limitation of SD prior itself that it only demonstrates significant advantages when handling highly ill-posed tasks [2, 8, 46]. Consequently, our proposed OSIRDiff is similarly affected by this limitation and performs well primarily at larger rescaling scales ( $>S$ ). In the future, we could explore the incorporation of shallow features into the VAE decoding process to enhance its fidelity, thereby enabling the OSIRDiff framework to be more applicable to small-scale rescaling tasks.

Table 4. Comparison of inference time and parameter sizes across methods.

	Time (s)	Total Parameters (M)	Trainable Parameters (M)
IRN	0.359	34.2	34.2
HCFLOW	0.363	7.24	7.24
VQIR	0.897	92.9	20.7
Ours	0.711	1352.5	63.2

## 6.2. Inference Time and Model Size

In Table 4, we compare the inference speed and parameter sizes of different methods. All tests are performed on an RTX 3090 using images with a resolution of  $1024 \times 1024$ . Due to leveraging the SD architecture, our method has the largest total number of parameters and the highest number of trainable parameters. However, since our approach only requires a single denoising step, its inference time does not increase significantly compared to other methods. The inference speed of our method even surpasses that of the VQGAN-based [4] method, i.e. the VQIR. This is because, compared to VAE, the latent space of VQGAN has a higher number of channels. Additionally, the nearest-neighbor search process in VQGAN incurs significant computational overhead, adversely affecting its inference speed. In the future, we plan to explore architecture distillation techniques to further reduce the size of our image rescaling model and improve its inference speed.

## 7. Conclusion

We propose a novel framework called OSIRDiff to address issues such as insufficient texture and semantic inaccuracies in extreme image rescaling. Specifically, we design a DFRM to achieve bidirectional mapping between HR features and LR images. Then, we utilize a pre-trained SD model to perform a single denoising step on the rescaled features, enhancing its perceptual

quality. Considering the non-uniform quality of the rescaled latent features, we propose a novel time-step alignment strategy to achieve a balance between fidelity and perceptual quality. Both qualitative and quantitative experiments demonstrate the superiority of our approach.

## References

- [1] Eirikur Agustsson and Radu Timofte. Ntire 2017 challenge on single image super-resolution: Dataset and study. In *IEEE Conference on Computer Vision and Pattern Recognition Workshops*, pages 126–135, 2017. 6
- [2] Chaofeng Chen, Shangchen Zhou, Liang Liao, Haoning Wu, Wenxiu Sun, Qiong Yan, and Weisi Lin. Iterative token evaluation and refinement for real-world super-resolution. In *AAAI Conference on Artificial Intelligence*, pages 1010–1018, 2024. 13
- [3] Keyan Ding, Kede Ma, Shiqi Wang, and Eero P Simoncelli. Image quality assessment: Unifying structure and texture similarity. *IEEE Transactions on Pattern Analysis and Machine Intelligence*, 44(5):2567–2581, 2020. 6
- [4] Patrick Esser, Robin Rombach, and Bjorn Ommer. Taming transformers for high-resolution image synthesis. In *IEEE Conference on Computer Vision and Pattern Recognition*, pages 12873–12883, 2021. 2, 13
- [5] Shuhang Gu, Andreas Lugmayr, Martin Danelljan, Manuel Fritsche, Julien Lamour, and Radu Timofte. Div8k: Diverse 8k resolution image dataset. In *IEEE International Conference on Computer Vision Workshop*, pages 3512–3516. IEEE, 2019. 6, 8
- [6] Edward J Hu, Phillip Wallis, Zeyuan Allen-Zhu, Yuanzhi Li, Shean Wang, Lu Wang, Weizhu Chen, et al. Lora: Low-rank adaptation of large language models. In *International Conference on Learning Representations*, 2022. 3
- [7] Jia-Bin Huang, Abhishek Singh, and Narendra Ahuja. Single image super-resolution from transformed self-exemplars. In *IEEE Conference on Computer Vision and Pattern Recognition*, pages 5197–5206, 2015. 6, 7
- [8] Zhaoyang Jia, Jiahao Li, Bin Li, Houqiang Li, and Yan Lu. Generative latent coding for ultra-low bitrate image compression. In *IEEE Conference on Computer Vision and Pattern Recognition*, pages 26088–26098, 2024. 2, 13
- [9] Minguk Kang, Richard Zhang, Connelly Barnes, Sylvain Paris, Suha Kwak, Jaesik Park, Eli Shechtman, Jun-Yan Zhu, and Taesung Park. Distilling diffusion models into conditional gans. *arXiv preprint arXiv:2405.05967*, 2024. 3, 5
- [10] Tero Karras, Samuli Laine, and Timo Aila. A style-based generator architecture for generative adversarial networks. In *IEEE Conference on Computer Vision and Pattern Recognition*, pages 4401–4410, 2019. 2
- [11] Tero Karras, Samuli Laine, Miika Aittala, Janne Hellsten, Jaakko Lehtinen, and Timo Aila. Analyzing and improving the image quality of stylegan. In *IEEE Conference on Computer Vision and Pattern Recognition*, pages 8110–8119, 2020. 2
- [12] Tero Karras, Miika Aittala, Timo Aila, and Samuli Laine. Elucidating the design space of diffusion-based generative

- models. *Advances in Neural Information Processing Systems*, 35:26565–26577, 2022. 3
- [13] Junjie Ke, Qifei Wang, Yilin Wang, Peyman Milanfar, and Feng Yang. Musiq: Multi-scale image quality transformer. In *IEEE International Conference on Computer Vision*, pages 5148–5157, 2021. 6
- [14] Heewon Kim, Myungsub Choi, Bee Lim, and Kyoung Mu Lee. Task-aware image downscaling. In *European Conference on Computer Vision*, pages 399–414, 2018. 1, 2
- [15] Jinmin Li, Tao Dai, Jingyun Zhang, Kang Liu, Jun Wang, Shaoming Wang, Shu-Tao Xia, et al. Boundary-aware decoupled flow networks for realistic extreme rescaling. *arXiv preprint arXiv:2405.02941*, 2024. 2
- [16] Shang Li, Guixuan Zhang, Zhengxiong Luo, Jie Liu, Zhi Zeng, and Shuwu Zhang. Approaching the limit of image rescaling via flow guidance. *arXiv preprint arXiv:2111.05133*, 2021. 2, 4
- [17] Yue Li, Dong Liu, Houqiang Li, Li Li, Zhu Li, and Feng Wu. Learning a convolutional neural network for image compact-resolution. *IEEE Transactions on Image Processing*, 28(3):1092–1107, 2018. 2
- [18] Jingyun Liang, Andreas Lugmayr, Kai Zhang, Martin Danelljan, Luc Van Gool, and Radu Timofte. Hierarchical conditional flow: A unified framework for image super-resolution and image rescaling. In *IEEE International Conference on Computer Vision*, pages 4076–4085, 2021. 1, 2, 6, 8, 9
- [19] Bee Lim, Sanghyun Son, Heewon Kim, Seungjun Nah, and Kyoung Mu Lee. Enhanced deep residual networks for single image super-resolution. In *IEEE Conference on Computer Vision and Pattern Recognition Workshops*, pages 136–144, 2017. 6, 8
- [20] Kingchao Liu, Xiwen Zhang, Jianzhu Ma, Jian Peng, et al. InstafLOW: One step is enough for high-quality diffusion-based text-to-image generation. In *The Twelfth International Conference on Learning Representations*, 2023. 3
- [21] Cheng Lu, Yuhao Zhou, Fan Bao, Jianfei Chen, Chongxuan Li, and Jun Zhu. Dpm-solver: A fast ode solver for diffusion probabilistic model sampling in around 10 steps. *Advances in Neural Information Processing Systems*, 35:5775–5787, 2022. 3
- [22] Siwei Ma, Xinfeng Zhang, Chuanmin Jia, Zhenghui Zhao, Shiqi Wang, and Shanshe Wang. Image and video compression with neural networks: A review. *IEEE Transactions on Circuits and Systems for Video Technology*, 30(6):1683–1698, 2019. 4
- [23] Chenlin Meng, Robin Rombach, Ruiqi Gao, Diederik Kingma, Stefano Ermon, Jonathan Ho, and Tim Salimans. On distillation of guided diffusion models. In *IEEE Conference on Computer Vision and Pattern Recognition*, pages 14297–14306, 2023. 3
- [24] Thuan Hoang Nguyen and Anh Tran. Swiftbrush: One-step text-to-image diffusion model with variational score distillation. In *IEEE Conference on Computer Vision and Pattern Recognition*, pages 7807–7816, 2024. 3
- [25] Zhihong Pan, Baopu Li, Dongliang He, Mingde Yao, Wenhao Wu, Tianwei Lin, Xin Li, and Errui Ding. Towards bidirectional arbitrary image rescaling: Joint optimization and cycle idempotence. In *IEEE Conference on Computer Vision and Pattern Recognition*, pages 17389–17398, 2022. 1
- [26] Chenyang Qi, Xin Yang, Ka Leong Cheng, Ying-Cong Chen, and Qifeng Chen. Real-time 6k image rescaling with rate-distortion optimization. In *IEEE Conference on Computer Vision and Pattern Recognition*, pages 14092–14101, 2023. 1
- [27] Robin Rombach, Andreas Blattmann, Dominik Lorenz, Patrick Esser, and Björn Ommer. High-resolution image synthesis with latent diffusion models. In *IEEE Conference on Computer Vision and Pattern Recognition*, pages 10684–10695, 2022. 2
- [28] Chitwan Saharia, Jonathan Ho, William Chan, Tim Salimans, David J Fleet, and Mohammad Norouzi. Image super-resolution via iterative refinement. *IEEE Transactions on Pattern Analysis and Machine Intelligence*, 45(4):4713–4726, 2022. 2
- [29] Tim Salimans and Jonathan Ho. Progressive distillation for fast sampling of diffusion models. In *International Conference on Learning Representations*, 2022. 3
- [30] Jiaming Song, Chenlin Meng, and Stefano Ermon. Denoising diffusion implicit models. In *International Conference on Learning Representations*, 2021. 3
- [31] Wanjie Sun and Zhenzhong Chen. Learned image downscaling for upscaling using content adaptive resampler. *IEEE Transactions on Image Processing*, 29:4027–4040, 2020. 1, 2
- [32] George Toderici, Lucas Theis, Nick Johnston, Eirikur Agustsson, Fabian Mentzer, Johannes Ballé, Wenzhe Shi, and Radu Timofte. CLIC 2020: Challenge on learned image compression, 2020, 2020. 6
- [33] Jianyi Wang, Kelvin CK Chan, and Chen Change Loy. Exploring clip for assessing the look and feel of images. In *AAAI Conference on Artificial Intelligence*, pages 2555–2563, 2023. 6
- [34] Jianyi Wang, Zongsheng Yue, Shangchen Zhou, Kelvin CK Chan, and Chen Change Loy. Exploiting diffusion prior for real-world image super-resolution. *arXiv preprint arXiv:2305.07015*, 2023. 2
- [35] Luozhou Wang, Shuai Yang, Shu Liu, and Ying-cong Chen. Not all steps are created equal: Selective diffusion distillation for image manipulation. In *IEEE International Conference on Computer Vision*, pages 7472–7481, 2023. 2, 5
- [36] Xintao Wang, Ke Yu, Shixiang Wu, Jinjin Gu, Yihao Liu, Chao Dong, Yu Qiao, and Chen Change Loy. Esrgan: Enhanced super-resolution generative adversarial networks. In *European Conference on Computer Vision Workshops*, pages 0–0, 2018. 6, 8
- [37] Zhou Wang, Alan C Bovik, Hamid R Sheikh, and Eero P Simoncelli. Image quality assessment: from error visibility to structural similarity. *IEEE Transactions on Image Processing*, 13(4):600–612, 2004. 6
- [38] Zhihao Wang, Jian Chen, and Steven CH Hoi. Deep learning for image super-resolution: A survey. *IEEE Transactions on Pattern Analysis and Machine Intelligence*, 43(10):3365–3387, 2020. 4

- [39] Hao Wei, Chenyang Ge, Zhiyuan Li, Xin Qiao, and Pengchao Deng. Towards extreme image rescaling with generative prior and invertible prior. *IEEE Transactions on Circuits and Systems for Video Technology*, 2024. 2, 6, 8
- [40] Rongyuan Wu, Lingchen Sun, Zhiyuan Ma, and Lei Zhang. One-step effective diffusion network for real-world image super-resolution. *arXiv preprint arXiv:2406.08177*, 2024. 10
- [41] Mingqing Xiao, Shuxin Zheng, Chang Liu, Zhouchen Lin, and Tie-Yan Liu. Invertible rescaling network and its extensions. *International Journal of Computer Vision*, 131(1): 134–159, 2023. 1, 2, 6, 8
- [42] Zhiseng Xiao, Karsten Kreis, and Arash Vahdat. Tackling the generative learning trilemma with denoising diffusion gans. In *International Conference on Learning Representations*, 2022. 3
- [43] Bingna Xu, Yong Guo, Luoqian Jiang, Mianjie Yu, and Jian Chen. Downscaled representation matters: Improving image rescaling with collaborative downscaled images. In *IEEE International Conference on Computer Vision*, pages 12237–12247, 2023. 2
- [44] Jinhai Yang, Mengxi Guo, Shijie Zhao, Junlin Li, and Li Zhang. Self-asymmetric invertible network for compression-aware image rescaling. In *AAAI Conference on Artificial Intelligence*, pages 3155–3163, 2023. 1
- [45] Tianwei Yin, Michaël Gharbi, Richard Zhang, Eli Shechtman, Fredo Durand, William T Freeman, and Taesung Park. One-step diffusion with distribution matching distillation. In *IEEE Conference on Computer Vision and Pattern Recognition*, pages 6613–6623, 2024. 3
- [46] Fanghua Yu, Jinjin Gu, Zheyuan Li, Jinfan Hu, Xiangtao Kong, Xintao Wang, Jingwen He, Yu Qiao, and Chao Dong. Scaling up to excellence: Practicing model scaling for photo-realistic image restoration in the wild. In *IEEE Conference on Computer Vision and Pattern Recognition*, pages 25669–25680, 2024. 13
- [47] Lvmin Zhang, Anyi Rao, and Maneesh Agrawala. Adding conditional control to text-to-image diffusion models. In *IEEE International Conference on Computer Vision*, pages 3836–3847, 2023. 2
- [48] Min Zhang, Zhihong Pan, Xin Zhou, and C-C Jay Kuo. Enhancing image rescaling using dual latent variables in invertible neural network. In *ACM International Conference on Multimedia*, pages 5602–5610, 2022. 2
- [49] Richard Zhang, Phillip Isola, Alexei A Efros, Eli Shechtman, and Oliver Wang. The unreasonable effectiveness of deep features as a perceptual metric. In *IEEE Conference on Computer Vision and Pattern Recognition*, pages 586–595, 2018. 6
- [50] Yulun Zhang, Kunpeng Li, Kai Li, Lichen Wang, Bineng Zhong, and Yun Fu. Image super-resolution using very deep residual channel attention networks. In *European Conference on Computer Vision*, pages 286–301, 2018. 6, 8
- [51] Wenliang Zhao, Lujia Bai, Yongming Rao, Jie Zhou, and Jiwen Lu. Unipc: A unified predictor-corrector framework for fast sampling of diffusion models. *Advances in Neural Information Processing Systems*, 36, 2024. 3
- [52] Hongkai Zheng, Weili Nie, Arash Vahdat, Kamyar Azizadenesheli, and Anima Anandkumar. Fast sampling of diffusion models via operator learning. In *International Conference on Machine Learning*, pages 42390–42402. PMLR, 2023. 3
- [53] Zhixuan Zhong, Liangyu Chai, Yang Zhou, Bailin Deng, Jia Pan, and Shengfeng He. Faithful extreme rescaling via generative prior reciprocated invertible representations. In *IEEE Conference on Computer Vision and Pattern Recognition*, pages 5708–5717, 2022. 2
- [54] Yiming Zhu, Cairong Wang, Chenyu Dong, Ke Zhang, Hongyang Gao, and Chun Yuan. High-frequency normalizing flow for image rescaling. *IEEE Transactions on Image Processing*, 32:6223–6233, 2022. 2